Physics of the Earth and Planetary Interiors 171 (2008) 374–386

Contents lists available at ScienceDirect

Physics of the Earth and Planetary Interiors

journal homepage: www.elsevier.com/locate/pepi

Thermomechanics of mid-ocean ridge segmentation

Eun-seo Choi[a,*], Luc Lavier[b], Michael Gurnis[a]

[a] Seismological Laboratory, California Institute of Technology, 1200 East California Boulevard, Pasadena, CA 91125, USA
[b] Institute for Geophysics, John A. and Katherine G. Jackson School of Geosciences, The University of Texas at Austin, J.J. Pickle Research Campus, Building 196 (ROC), 10100 Burnet Road (R2200), Austin, TX 78758-4445, USA

ARTICLE INFO

Article history:
Received 25 September 2007
Received in revised form 30 June 2008
Accepted 4 August 2008

Keywords:
Mid-ocean ridge propagation
Ridge tip interaction
Thermal stress
Elasto-visco-plastic rheology

ABSTRACT

The mechanics responsible for the initiation of the orthogonal pattern characterizing mid-ocean ridges and transform faults are studied using numerical models. The driving forces are thermal stresses arising from the cooling of young oceanic crust and extensional kinematic boundary conditions. Thermal stress can exert ridge-parallel tension comparable in magnitude to spreading-induced tension when selectively released by ridges and ridge-parallel structure. Two modes of ridge segment growth have been identified in plan view: an overlapping mode where ridge segments overlap and bend toward each other and a connecting mode where two ridge segments are connected by a transform-like fault. As the ratio of thermal stress to spreading-induced stress (γ) increases, the patterns of localized plastic strain change from the overlapping to connecting mode. The orthogonal pattern marks the transition from one mode to the other. Besides the amount of stress from each driving force, the rate of stress accumulation is crucial in determining the emergent pattern. This rate-dependence is characterized by the spreading rate normalized by a reference-cooling rate (Pe'). When Pe' is paired with the ratio of thermal stress to the reference spreading-induced stress (γ'), they unambiguously define stability fields of the two modes. The obliquely connecting, the orthogonally connecting, and the overlapping mode are similar to ridge-transform fault intersections observed in ultra-slow, slow to intermediate, and fast spreading centers, respectively. The patterns are also sensitive to the strain weakening rate. Fracture zones were created in part as a response to thermal stress.

1. Introduction

Mid-ocean ridges and transform faults intersect to make various patterns, one being the idealized "orthogonal" pattern prominently characterizing plate boundaries. However, the processes responsible for the emergence and stability of such patterns remain poorly understood. Mid-ocean ridges are a hierarchical system of discontinuous ridge segments offset by different types of discontinuities (Macdonald et al., 1991). Segmentation at different scales has invited multiple theories for their origin (e.g., Macdonald et al., 1991; Phipps Morgan, 1991; Abelson and Agnon, 1997). It remains unclear whether the hierarchy is the product of different mechanisms working at different scales or the scale-dependence of a single mechanism. While the overall trend of mid-ocean ridges is imposed by the geometry of continental breakup and passive margin formation, the geometric coincidence between passive margins and mid-ocean ridges led Wilson (1965) to first propose that transform faults are inherited from preexisting structures. Subsequent studies proposed that stepping half-grabens (e.g., Cochran and Martinez, 1988; McClay and Khalil, 1998), segmented gravity and magnetic anomalies (e.g., Behn and Lin, 2000), or segmented weak regions (e.g., Watts and Stewart, 1998) along passive margins ultimately lead to the discontinuities found along mid-ocean ridges. However, other observations support the hypothesis that the orthogonal ridge-transform system is emergent and not solely due to preexisting conditions. Sandwell (1986) presented three lines of evidence supporting this hypothesis: (1) that single straight ridges can develop into an orthogonal pattern, (2) the existence of zero offset fracture zones, and (3) a positive correlation between ridge segment length and spreading rate.

Differences in the rate of energy dissipation between ridge segments and transform faults have been suggested to lead to the orthogonal pattern (Lachenbruch, 1973; Froidevaux, 1973). According to this theory, energy dissipation can be more efficient at a spreading center than a transform fault and, as a result, the minimized ridge segment length by an orthogonal pattern results in the least energy dissipation. However, it was subsequently shown that the orthogonal pattern could be created without assuming higher energy dissipation at the spreading centers (Oldenburg and Brune, 1975). Atwater and MacDonald (1977) also questioned the validity

* Corresponding author. Tel.: +1 626 395 6971; fax: +1 626 564 0715.
E-mail address: ces74@gps.caltech.edu (E.-s. Choi).

0031-9201/$ – see front matter © 2008 Elsevier B.V. All rights reserved.
doi:10.1016/j.pepi.2008.08.010

of the minimum energy dissipation argument based on inconsistency with observations.

The observation of the oblique fabric of normal faults around ridge-transform fault intersections is such that they must result from both a ridge normal and a ridge parallel component of stress (Gudmundsson, 1995). Gudmundsson (1995) proposed the expansion of a plate's perimeter as an origin of ridge-parallel tension. However, Gudmundsson's hypothesis does not address the possibility that each ridge segment can grow instead of forming fracture zones, and the observed fabric often requires a low degree of mechanical coupling across transform faults and the associated shear stresses (e.g., Fujita and Sleep, 1978; Fox and Gallo, 1984; Grindlay and Fox, 1993; Behn et al., 2002). Also, changes in the direction of plate motion was suggested to lead to the development of the orthogonal pattern (Menard and Atwater, 1969), but this mechanism is not sufficiently general to explain most present mid-ocean ridge systems where changes in plate direction have been limited. A more plausible source for ridge-parallel tension is the cooling of oceanic lithosphere. Thermal cooling stresses make a significant contribution to the stress state of oceanic plates. Heuristic calculations (Collette, 1974), a calculation based on a plate cooling model (Turcotte, 1974; Sandwell, 1986), the presence of near-ridge seismicity (Wiens and Stein, 1984; Bergman and Solomon, 1984), and geoid anomalies over fracture zones (Parmentier and Haxby, 1986; Haxby and Parmentier, 1988) all indicate that thermal stresses can contribute significantly to a ridge parallel component of stress. Thermal stresses are isotropic, but mid-ocean ridges themselves and numerous ridge parallel faults can release thermal stresses in a selective (i.e., ridge-perpendicular) direction when these structures form (Fig. 1). Therefore, the resultant unreleased stress due to cooling would be dominated by the ridge-parallel component.

Analog experiments using paraffin wax have been more successful than others in studying the emergence of patterns similar to those found at mid-ocean ridges. Oldenburg and Brune (1972) designed an experiment in which the surface of molten wax was chilled by a fan. The basin containing the molten wax was heated from below. One side of the solidified wax is pulled to generate extensional stresses. They observed the spontaneous growth of an orthogonal system of ridge, transform faults, and fracture zones with characteristics similar to natural systems. They concluded that the orthogonal ridge-transform fault system is a preferred mode of plate separation and that a weak shear resistance on transform faults is required for the system's stability (Oldenburg and Brune, 1975). Based on the high volume change of cooling wax, Sandwell (1986) interpreted that orthogonally intersecting structures made in wax originated as a mechanism to release thermal stress. Wax was also used to study the microplate formation in a fast-spreading environment (Katz et al., 2005).

The success of the wax models implies that the orthogonal pattern of ridges and transform faults are caused by a combination of spreading and thermal stresses. However, to more fully understand the physics while adding additional processes critical for mid-ocean ridges, we turn to a numerical approach. Using numerical simulations, known representative values for the Earth's material can be directly used in models. In addition, numerical experiments allow for a better control on testable mechanisms and a wide range of parameter values. Numerical models can also be used to make explicit predictions of geophysical observations such as bathymetry and gravity.

Our goal is to reveal the mechanism responsible for the emergence of the orthogonal pattern at mid-ocean ridges using a 3D numerical method. Our approach is distinguished from previous 3D numerical models for the mid-ocean ridge system that treated transform faults as pre-existing structures or as boundary conditions (e.g., Parmentier and Phipps Morgan, 1990; Furlong et al., 2001). In our study, transform faults and fracture zones, as well as ridge segments are all created as a response of a mechanical sys-

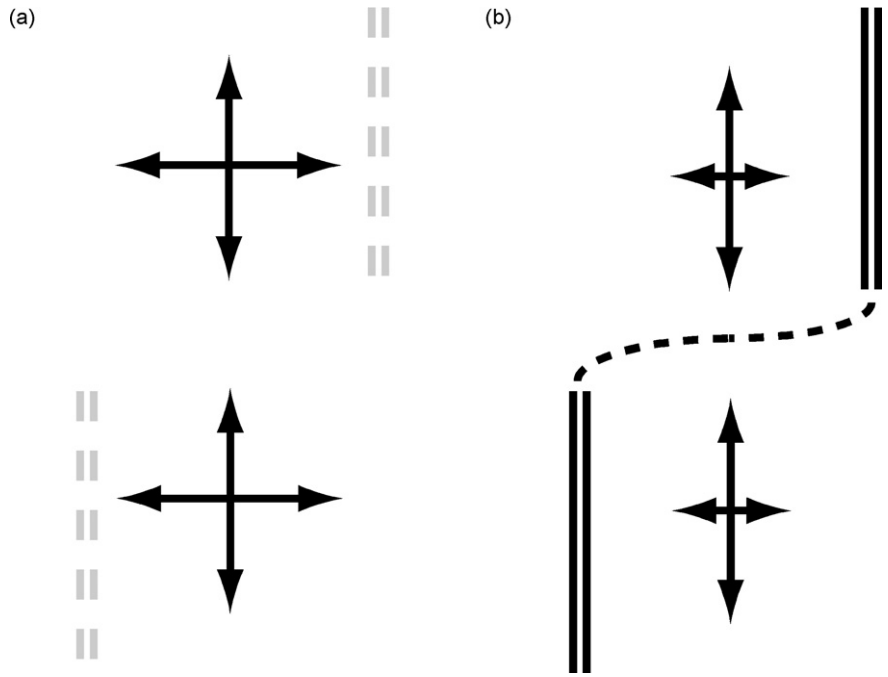

Fig. 1. Ridge segments and other ridge-parallel structures can release thermal stress in the ridge-normal direction, while leaving ridge-parallel residual stresses. Arrows represent the direction and the magnitude of components of thermal stresses aligned along ridge-perpendicular and ridge-parallel directions. (a) Before ridge segments are created, thermal stress is isotropic and its horizontal components are equal in magnitude. The future location of ridge segments are marked by the pairs of gray dashed lines. (b) The ridge-parallel component becomes dominant when the ridge-normal principal stress is released by the formation of ridge segments (pairs of solid lines). A possible trace of a structure connecting the ridge segments is denoted by a dased curve.

tem to given initial and boundary conditions. A 2D elastic damage model has been developed (Hieronymus, 2004), but differed from ours in terms of geometry, material properties, and the physical processes incorporated. We focus our attention on the first order segments and discontinuities, corresponding to ridge segments and transform faults, respectively (Macdonald et al., 1991).

2. Numerical method

We use SNAC, an explicit Lagrangian finite difference code, to model the dynamics associated with the initiation of ridge-transform fault systems in three-dimensions. SNAC is a framework-based software, using the energy-based finite difference method to solve the force balance equation for elasto-visco-plastic materials (Bathe, 1996). The details of the algorithm are presented in Appendix A.

Implementing the elasto-visco-plastic material type in SNAC is crucial because localization of plastic strain occurring due to bifurcation inherent to plasticity can be regarded as a large-scale manifestation of localized deformation like fault zones. Propagating ridge segments, transform faults, and fracture zones are all represented by localized plastic strain. In addition, a vertical gradient of temperature determines the transition from cold plastic material near the top to hot Maxwell viscoelastic material below.

Cooling of newly formed lithosphere is one of the key phenomena for modeling mid-ocean ridge system. SNAC computes thermal diffusion using the same type of solver as the solution of the momentum equation. Temporal variation of the temperature field contributes to the isotropic components of stress through thermal expansion and contraction.

We use an elasto-visco-plasticity (EVP) model in which total strain is the sum of contributions from elastic, viscous, and plastic components (e.g., Albert et al., 2000). This material model assumes a Maxwell viscoelastic rheology at all times, but if the stress exceeds a specified criterion before being relaxed then yielding occurs. We use a Mohr–Coulomb yield criterion and a power-law viscosity (Lavier and Buck, 2002). The EVP constitutive relations allow a wide range of material behavior to emerge: elastoplastic when temperature is low and viscoelastic at high temperatures. To induce localization, a strain-weakening rule is applied to the yield criteria. The rule is usually a piecewise linear function of accumulated plastic strain such that the plastic material properties (cohesion and angle of internal friction) decrease with increasing plastic strain (Lavier et al., 2000). In addition, elements are assigned initial finite plastic strain so that localization initiates from those elements. In this way, we can prevent the occurrence of localized plastic deformation adjacent to the boundary of the computational domain.

3. Model setup

We model a hot block of oceanic lithosphere that cools while it is stretched at a given spreading rate. Spreading initiates ridge segments, which in turn releases accumulating thermal stress only in the ridge-normal direction. The ensuing process is governed by given parameters and boundary conditions.

The domain is 60 km × 5 km × 60 km and is discretized into 1-km cubic elements (Fig. 2a). Initial temperature is uniformly 1300 °C except along the top surface, where temperature is 0 °C. The top surface remains isothermal at 0 °C, while the bottom surface has a composite boundary condition. By the zero heat flux condition, heat is lost until the bottom temperature decreases to 750 °C; thereafter the bottom temperature is kept at 750 °C. These thermal initial and boundary conditions are intended to be those of hypothetically pristine oceanic lithosphere that is about to cool and extend. Heat fluxes are zero on all the side walls. We assume that the distinctive thermal structure of slow and fast mature ridges result from long-term spreading, not given initially. In reality, the thickness of lithosphere is not constant over the distance of 60 km across a spreading center. However, we assumed it to be initially uniform in order to exclude the influence of pre-existing structures. If the variation in lithospheric thickness is predefined, so would the pattern we seek because the thinnest part will develop into spreading centers unless other perturbations are considered.

Velocity boundary conditions are applied to two sidewalls while the other two are free-slip (Fig. 2b). The bottom surface was supported by a frictionless denser foundation called a Winkler foundation (e.g., see p. 95 in Watts, 2001). This bottom boundary condition works in such a ways that normal tractions are applied in the opposite direction to the deflection of the bottom surface and with a magnitude given by the surface integral of pressure change, $(\rho_m - \rho_f) g \Delta h(x)$, where ρ_m is the mantle density at the bottom of the domain, ρ_f is the assumed density of the foundation, g is the gravitational acceleration, and $\Delta h(x)$ is the change in the vertical coordinates at location x. For simplicity, we assume $(\rho_m - \rho_f)$ is fixed at at 50 km/m^3. The two tangential components of traction are set to be zero.

Two ridge segments develop as narrow regions of localized strain. Strain localization initiates from two "seeds", elements with non-zero plastic strain and offset by 30 km in both horizontal directions (Fig. 2a). In addition, we assumed a piecewise linear function in strain weakening such that 100 MPa of cohesion is reduced to 50 MPa at 1% plastic strain, and to 10 MPa at 3%. All the plastic parameters (cohesion, internal friction angle, and dilation angle) are kept the same after plastic strain grows larger than 3%. Unfortunately, strain weakening is poorly constrained by geological

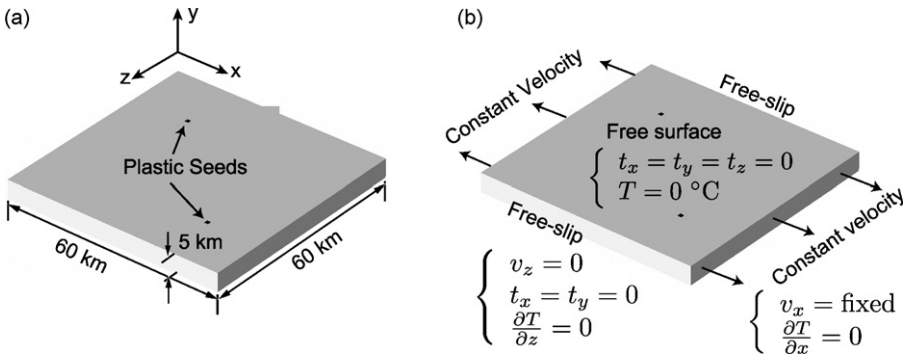

Fig. 2. Geometry of the model domain. (a) 60 km × 5 km × 60 km domain with equal 1 km grid spacing in each direction. Two plastic seeds, controlling initial localization, are embedded with 30 km separation in the x and z directions. (b) Two side surfaces normal to the x axis are pulled at a constant velocity. The other two sides, normal to z axis, have free-slip boundary conditions, where the normal velocity (v_z) and tangential components of traction (t_x and t_y) are 0. Zero heat flux is assumed for all the side walls, but the top surface temperature is fixed at 0 °C. See the text for thermal and mechanical boundary conditions for the bottom surface.

Table 1
Parameter values

Model	v (cm/year)	α_v ($\times 10^{-5}$ K^{-1})	κ ($\times 10^{-6}$ m^2/s)	$\epsilon_{ps,1}$	C_1 (MPa)	$\epsilon_{ps,2}$
Base	3	6	1.12	0.01	50.00	0.03
1	1	6	1.12	0.01	50.00	0.03
2	10	6	1.12	0.01	50.00	0.03
3	3	5.49	1.12	0.01	50.00	0.03
4	3	6.51	1.12	0.01	50.00	0.03
5	3	6	0.915	0.01	50.00	0.03
6	3	6	1.36	0.01	50.00	0.03
7	2	6	1.12	0.01	50.00	0.03
8	4	6	1.12	0.01	50.00	0.03
9	3	5.76	1.12	0.01	50.00	0.03
10	3	6.24	1.12	0.01	50.00	0.03
11	3	6	1.02	0.01	50.00	0.03
12	3	6	1.22	0.01	50.00	0.03
13	2.5	6	1.12	0.01	50.00	0.03
14	3.5	6	1.12	0.01	50.00	0.03
15	3	5.88	1.12	0.01	50.00	0.03
16	3	6.12	1.12	0.01	50.00	0.03
17	3	6	1.07	0.01	50.00	0.03
18	3	6	1.17	0.01	50.00	0.03
19	3.3	6.6	1.12	0.01	50.00	0.03
20	3.03	6.06	1.12	0.01	50.00	0.03
21	3.3	6	1.232	0.01	50.00	0.03
22	2.7	5.4	1.12	0.01	50.00	0.03
23	2.97	5.94	1.12	0.01	50.00	0.03
24	2.7	6	1.008	0.01	50.00	0.03
25	4.68	6.6	1.12	0.01	50.00	0.03
26	4	6.34	1.12	0.01	50.00	0.03
27	3.73	6.24	1.12	0.01	50.00	0.03
28	2.27	5.76	1.12	0.01	50.00	0.03
29	2	5.69	1.12	0.01	50.00	0.03
30	1.34	5.49	1.12	0.01	50.00	0.03
31	2.5	5.65	1.12	0.01	50.00	0.03
32	2.0	5.46	1.12	0.01	50.00	0.03
33	1.34	5.19	1.12	0.01	50.00	0.03
34	2.00	5.19	1.12	0.01	50.00	0.03
35	2.50	5.19	1.12	0.01	50.00	0.03
36	1.34	4.90	1.12	0.01	50.00	0.03
37	2.00	4.90	1.12	0.01	50.00	0.03
38	2.50	4.90	1.12	0.01	50.00	0.03
W1	3	6	1.12	0.01	50.00	0.02
W2	3	6	1.12	0.02	50.00	0.05
W3	3	6	1.12	0.01	25.00	0.03
W4	3	6	1.12	0.01	75.00	0.03
W5	3	6	1.12	0.01	50.00	0.03
W6	3	6	1.12	0.01	50.00	0.03
W7	3	6	1.12	0.01	43.75	0.03
W8	3	6	1.12	0.01	56.25	0.03

Density = 2950 kg/m^3; Lame's constants (λ, μ) = 30 GPa, respectively; $\epsilon_{ps,0} = 0$, $C_0 = 100$ MPa, $C_2 = 10$ MPa; $n = 3$, $Q = 380$ kJ/mol, and $A = 1.73 \times 105$ (Pa s)$^{1/n}$ for viscosity.

observations (Scholz, 2002; Lavier et al., 2000). Parameters related to the constitutive law are listed in Table 1.

3.1. Base model and its variations

One model is referred to as the "base case" and produced a nearly orthogonal transform fault that connected ridge segments (Fig. 3). The imposed constant spreading rates are equivalent to time-varying forces required to maintain the spreading rate (Lavier and Buck, 2002; Gurnis et al., 2004). The spreading-parallel component of this force (F_x), as a function of time, is useful for monitoring the change in the state of stress. F_x for the base case (Fig. 3a) shows that the system was initially in equilibrium with 1.22×10^9 N/m of external force remaining invariant for about 7000 years. The pattern of localization was determined during this phase, and it was not affected by subsequent deformation. When the subsurface layer cooled sufficiently, the exponentially increased temperature-dependent viscosity rendered the layer elastic and thus the overall stiffness of the model increased (Fig. 3b). Consequently, F_x increases in response to this change after 7000 years, manifest as a bulge in F_x versus time. As deformation due to spreading and thermal stress continues, the cooled portions of the layer yield and become weaker beneath ridge segments (Fig. 3e). This leads to the decrease of F_x (Fig. 3a).

The total elapsed time, about 15 kyears, was insufficient to develop into the morphology seen at mature mid-ocean ridges, as shown with topography along with the deformed mesh and accumulated plastic strain (Fig. 4). However, it shows the deepening trend of bathymetry away from ridge segments and troughs along ridge-normal localized bands, consistent with an actual ridge-transform fault intersection. The curvature of zones of localized strain at the inner corner is consistent with the fabric of structures observed at slow spreading ridge-transform fault intersections (Fox and Gallo, 1984).

Models varied from the base case in terms of their pattern of localization. The patterns could be grouped based on their geometry into two modes: "connecting" and "overlapping" (Fig. 5). They are end members of the modes of interaction between two mutually approaching ridge segments. Connecting modes are further characterized by the angle θ between the connecting segment and the

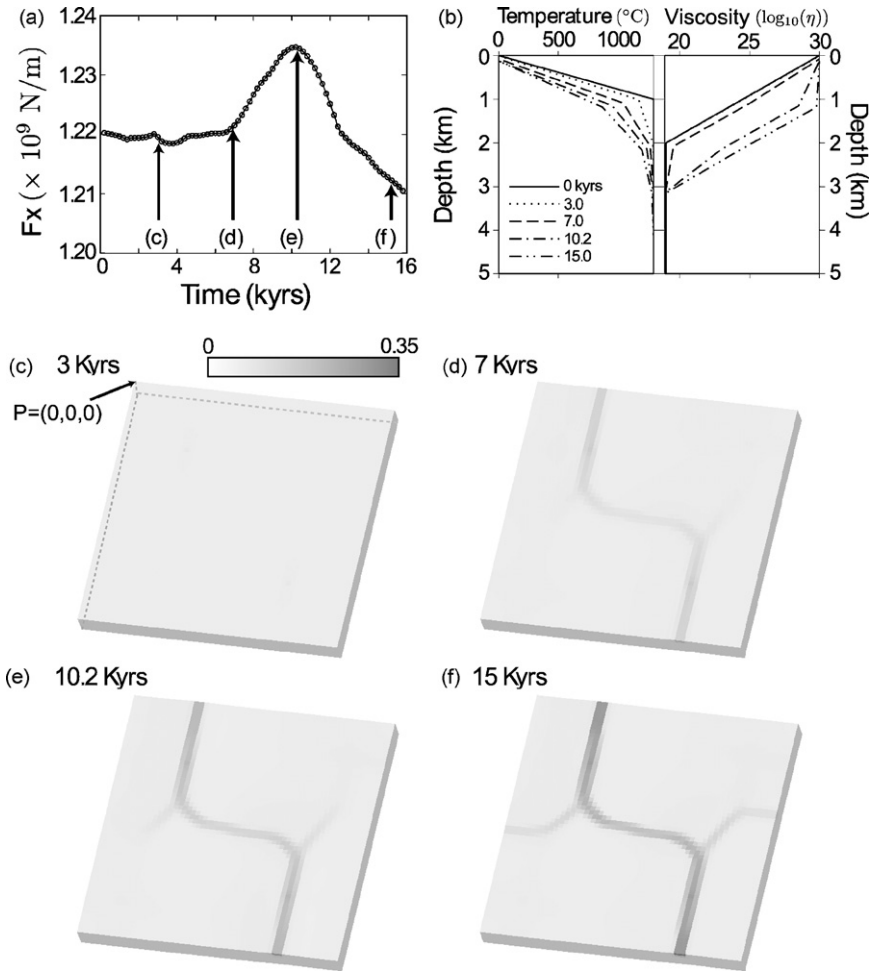

Fig. 3. (a) F_x, force required to extend the domain at the applied velocity in the x-direction as a function of time. (b) Depth profiles of temperature and viscosity are taken at the point P marked in (a) and compared at different time steps (0, 3, 7, 10.2, and 15 kyears). The rise in F_x at ~7 kyears coincides with the cooling and significant increase in viscosity of the subsurface (1–2 km deep) layer. 3D rendering of the second invariant of plastic strain at the same set of time steps: (c) 3 kyears, (d) 7 kyears, (e) 10.2 kyears, and (f) 15 kyears.

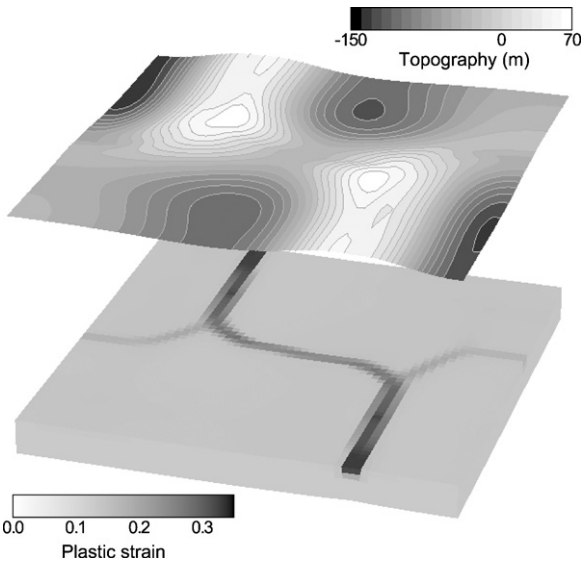

Fig. 4. A 3D representation of the surface topography from the base model at 15 kyears on top of the model domain. Plastic strain on the surface of the model domain indicated through grey scale shading.

ridge-normal direction; θ ranges from 0° to 45°, and the orthogonal pattern, corresponding to $\theta = 0°$, falls in the middle of the morphological range from high-θ connecting modes to overlapping modes.

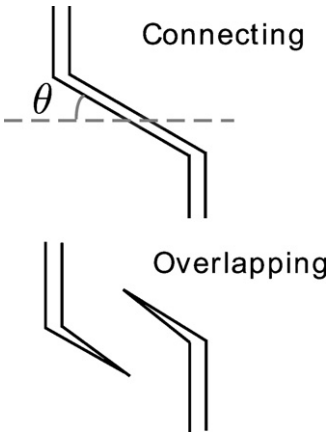

Fig. 5. Modes of interaction between two mutually approaching ridge segments. The orthogonal ridge-transform fault geometry is a special case of the "connecting" mode. The angle, θ, is used as a measure of a connecting pattern's orthogonality spanning the range 0–45°.

To assess quantitatively the relative influence of thermal stress to spreading-induced stress on the appearance of localization patterns, we introduce a dimensionless number γ. γ is defined as the ratio of the first invariant of thermal stress to the first invariant of spreading-induced stress:

$$\gamma = \frac{|I_\sigma^{\text{therm}}|}{|I_\sigma^{\text{spr}}|}. \tag{1}$$

Spreading-induced stress is given by constitutive relations for linear isotropic elasticity:

$$\sigma_{ij}^{\text{spr}} = \lambda\delta_{ij}\epsilon_{kk}^{\text{spr}} + 2\mu\epsilon_{ij}^{\text{spr}}, \tag{2}$$

where λ and μ are Lame's constants. Thermal stress is given as (e.g., Boley and Weiner, 1960):

$$\sigma_{ij}^{\text{spr}} = -(3\lambda + 2\mu)\delta_{ij}\alpha_{\text{l}}(T - T_0), \tag{3}$$

where α_{l} is the linear thermal expansion coefficient, T is temperature, and T_0 is the reference temperature. When extension in one horizontal direction and zero-strain in the other two directions is assumed, extensional stresses are, from (2),

$$\begin{aligned}\sigma_{11}^{\text{spr}} &= \lambda(\epsilon_{11}^{\text{spr}} + \epsilon_{22}^{\text{spr}} + \epsilon_{33}^{\text{spr}}) + 2\mu\epsilon_{11}^{\text{spr}} = (\lambda + 2\mu)\epsilon_{11}^{\text{spr}} \\ \sigma_{22}^{\text{spr}} &= \lambda\epsilon_{11}^{\text{spr}} \\ \sigma_{33}^{\text{spr}} &= \lambda\epsilon_{11}^{\text{spr}}\end{aligned} \tag{4}$$

Then, the first invariant of spreading-induced stress becomes:

$$I_\sigma^{\text{spr}} = \sigma_{11}^{\text{spr}} + \sigma_{22}^{\text{spr}} + \sigma_{33}^{\text{spr}} = (3\lambda + 2\mu)\epsilon_{11}^{\text{spr}}. \tag{5}$$

The first invariant of thermal stress is obtained from (3):

$$I_\sigma^{\text{therm}} = \sigma_{11}^{\text{therm}} + \sigma_{22}^{\text{therm}} + \sigma_{33}^{\text{therm}} = -(3\lambda + 2\mu)\alpha_{\text{v}}(T - T_0), \tag{6}$$

where α_{v} is the volumetric thermal expansion coefficient and is equal to $3\alpha_{\text{l}}$. Substituting (5) and (6) into (1) and taking the absolute value, we obtain

$$\begin{aligned}\gamma &= \frac{|(3\lambda + 2\mu)\alpha_{\text{v}}(T - T_0)|}{|(3\lambda + 2\mu)\varepsilon_{11}^{\text{spr}}|} = \frac{|\alpha_{\text{v}}(T - T_0)|}{\epsilon_{11}^{\text{spr}}} \\ &= \frac{|\alpha_{\text{v}}(\kappa\nabla^2 T)\,\Delta t|}{\dot{\epsilon}_{11}^{\text{spr}}\,\Delta t} \approx \frac{\alpha_{\text{v}}(\kappa\,\Delta T/D^2)}{\dot{\epsilon}_{11}^{\text{spr}}} = \frac{\kappa\alpha_{\text{v}}\,\Delta T}{\dot{\epsilon}_{11}^{\text{spr}} D^2},\end{aligned} \tag{7}$$

where $\dot{\epsilon}_{11}^{\text{spr}}$ is the strain rate associated with a half-spreading rate, Δt is the characteristic time of thermal diffusion, ΔT is the absolute temperature difference between surface and bottom, κ is the thermal diffusivity, D is the thickness of the domain. $\dot{\epsilon}_{11}^{\text{spr}}$ can be further approximated as v/L, where v is the half-spreading rate and L is the width of the domain:

$$\gamma = \frac{\kappa\alpha_{\text{v}}L\ \Delta T}{vD^2}. \tag{8}$$

When γ is defined as in (8), it represents the relative importance of conductive cooling with respect to spreading in determining the dominant state of stress for emergent oceanic lithosphere although it is not the stress ratio itself. Since the domain geometry (D and L) and the temperature initial condition (ΔT) are common to all the models, we vary the remaining three parameters, v, α_{v}, and κ to determine their influence on the pattern of localization.

Another measure of the system is introduced because the same value of γ can be achieved by different values of parameters that are varied in the same proportion. Those models with the same γ but different parameters can produce considerably different patterns because the growth rates of stresses from cooling and spreading are different even for the proportionally varied parameters. The absolute value of rates is important because the material strength governed by plasticity is finite. So, we use the Peclet number as another measure of the system which we physically interpret here as the ratio of forced spreading rate (v) to cooling rate (κ/D). To ensure that separate measures of each process are not inherently correlated by sharing common parameters, we compute them with respect to reference values of v and κ/D. Thus, a pair of non-dimensional numbers, and γ' and Pe', are defined as

$$\gamma' = \frac{\kappa\alpha_{\text{v}}L\ \Delta T}{v_{\text{ref}}D^2}, \tag{9}$$

$$Pe' = \frac{vD_{\text{ref}}}{\kappa_{\text{ref}}}, \tag{10}$$

where v_{ref} is 3 cm/year, κ_{ref} is 10^{-6} m^2/s, and D_{ref} is 5 km.

Strain weakening during plastic deformation is characterized by a reduction in cohesion, $C(\epsilon_{\text{ps}})$, as plastic strain (ϵ_{ps}) accumulates. We define a dimensionless number, ω, as follows:

$$\omega = 1.0 - \frac{\int C(\epsilon_{\text{ps}})\,\mathrm{d}\epsilon_{\text{ps}}}{C_{\text{ref}}\epsilon_{\text{ps},2}^{\text{ref}}}, \tag{11}$$

where C_{ref} is a reference value of cohesion, and $\epsilon_{\text{ps},2}^{\text{ref}}$ is a reference value of accumulated plastic strain where cohesion becomes 10% of its initial value (Fig. 6). C_{ref} and $\varepsilon_{\text{ps},2}^{\text{ref}}$ are 100 MPa and 3%, respectively. ω is proportional to the normalized work per unit volume done to reduce cohesion until plastic strain reaches a given value, $\epsilon_{\text{ps},2}$. In this study, the initial value of cohesion (C_0) and $\epsilon_{\text{ps},2}$ are always equal to C_{ref} and $\epsilon_{\text{ps},2}^{\text{ref}}$. If ω is higher than the base model, then more work would have been done to reduce cohesion; such a model ends up with lower cohesion even with the same amount of accumulated plastic strain. Table 1 lists values of all model parameters.

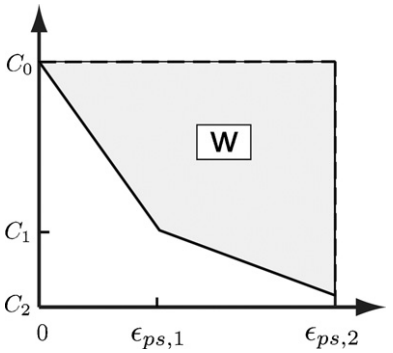

Fig. 6. The piecewise linear variation of cohesion as a function of accumulated plastic strain (ϵ_{ps}). Two-stage weakening was assumed in this study. ω, the work per unit volume done to reduce 90% of the initial cohesion, is used to quantify different weakening rules. C_0 and C_2 are 100 and 10 MPa, respectively, for all the models.

4. Results

We group models either with different γ and the same weakening rates (base case to model 38 in Table 1) or models with the same γ but different strain weakening rules (W1–W8).

4.1. Variation of γ

Using a subset of models with the same weakening rate (base case to model 38 in Table 1), localization patterns show a clear trend in the modes of interaction between ridge segments when arranged in order of increasing γ (Fig. 7). Patterns corresponding to relatively high γ (>0.24) are those of oblique spreading ridges. For the highest γ, corresponding to the strongest influence of thermal stress, two propagating segments are connected by a 45°-oblique ridge segment. θ decreases as γ becomes smaller and thus the spreading-

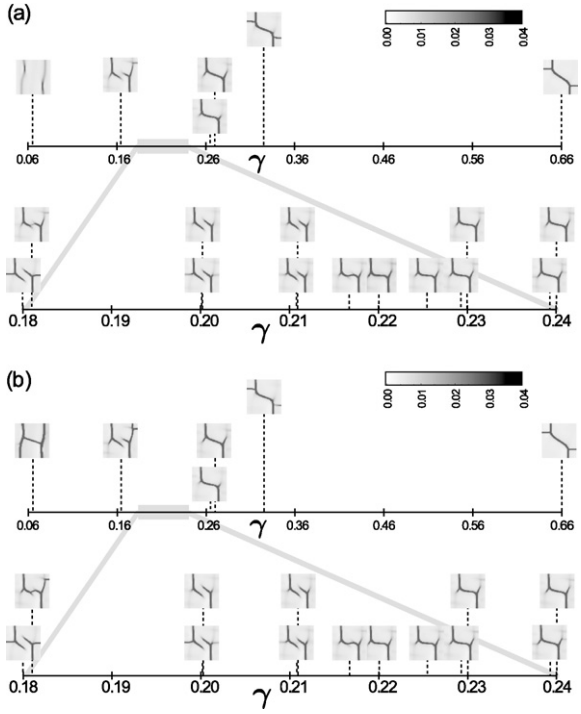

Fig. 7. Patterns of localized plastic strain, made on the top surface of models, are arranged in order of increasing γ. The patterns were captured (a) after 10.6 kyears and (b) after a given amount of spreading-induced strain, 0.535%. As γ increases, the mode of interaction between two mutually approaching ridge segments changes from oblique rifting through orthogonal rifting to overlapping-bending.

induced stress becomes stronger. Eventually, a nearly orthogonal pattern emerges within a narrow range of γ, from 0.22 to 0.23. When γ becomes smaller than 0.22, two ridge segments grow, overlap, and then bend toward each other. When the spreading-induced stress becomes even stronger ($\gamma < 0.1$), each segment propagates through the domain instead of bending or being connected by a shear band. The same trend is observed in both results after a constant time (Fig. 7a) or after constant extension (Fig. 7b).

When the force associated with spreading is plotted as a function of extension, we find two clearly divided populations of curves that correspond to the connecting and overlapping modes (Fig. 8). In terms of the rise time of F_x, the base model falls on the boundary between these two groups. The differences in the shape of the

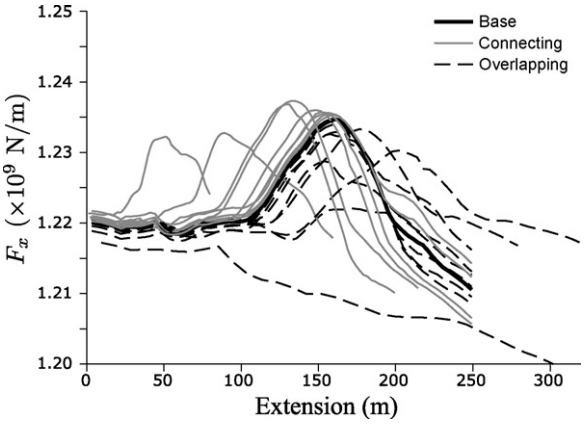

Fig. 8. For various models, F_x as a function of amount of extension. The base model (thick solid line) forms a boundary between curves for models in connecting modes (thin gray solid lines) and those models exhibiting overlapping modes (thin dashed lines).

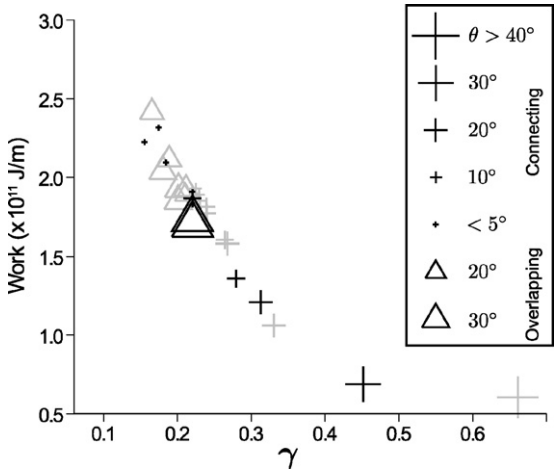

Fig. 9. Work done by the external extension until the peak in F_x versus γ for models with a single parameter (ν, α, or κ) varied from the base model (gray symbols) and those with two parameters varied simultaneously (either ν and α, or ν and κ, black symbols). Work and γ show an overall negative correlation. Models with connecting-mode patterns (crosses) show an approximately monotonic increase in θ as γ increases and work decreases. However, the modes of deformation and θ appear mixed in the low range of γ, indicating that γ and work cannot be unique indicators of emerging patterns. The overlapping-mode models (triangles) exhibit neither a broad variation in θ nor a one-to-one relation between work and γ.

curves in Fig. 8 can be quantified when the curves are integrated over their extended distance. The portion of the F_x curves after the peak does not exhibit a clear distinction between modes as before the peaks; consequently, we integrate F_x from 0 to the extension corresponding to the peak of F_x. The integrated values have units of work per unit length. When only one of the parameters ν, α, or κ was varied from the base model, the work decreases with increasing γ (gray symbols, Fig. 9). As γ decreases and the work increases, the angle between the connecting segment and the spreading direction (θ, Fig. 5) decreases, marking the transition to the overlapping mode at its minimum. Among models in the overlapping-mode, the correlation between work or γ and θ is not as clear. When two parameters (ν and α, or ν and κ) are varied simultaneously, models do not show systematic variations in mode or θ (black symbols, Fig. 9). Modes and the values of are mixed in the low-γ ranges. Thus, γ and work cannot uniquely predict the emerging pattern for all the models even though there is an obvious correlation.

The inability of predicting the emergent pattern is resolved when the Peclet number is considered as well, as shown when γ' is varied against Pe'. Since Pe' is a separate measure of the spreading rate with respect to a reference cooling rate, we are able to separate the two rate-dependent processes that are inherent in γ. All the models with the same weakening rate are plotted in Fig. 10. In contrast to the previous work versus γ plots, here the domains of each mode can be clearly divided. The boundary between the two modes that define the orthogonal pattern can be roughly traced along a single curve. The variation in θ is also systematic within the connected-mode domain. For a given spreading rate (constant Pe'), θ increases as thermal stress becomes dominant; for a given set of cooling-related parameters (constant γ'), θ increases as spreading becomes slower. The inferred stable region of orthogonal patterns suggests that when spreading rate is sufficiently small the overlapping mode is unable to form, regardless of γ'.

The transition from one faulting pattern to another occurred at specific values of Pe', which was confirmed by a suite of higher resolution models. We solved models on a mesh with half the horizontal grid spacing. The vertical resolution was not changed to maintain the same cooling rate with the original models and γ' was fixed at

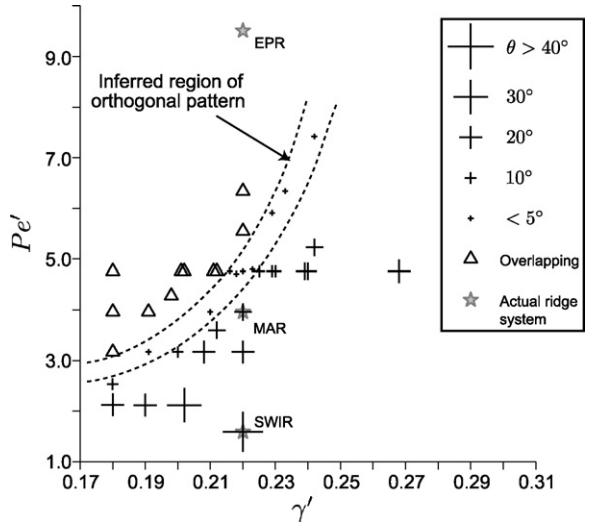

Fig. 10. Plot of Pe' versus γ'. The domain of connecting and overlapping mode is well defined and the boundary between them defines the stability field of the orthogonal pattern. Within the connecting-mode domain, the variation in θ is systematic: θ becomes smaller as the values of Pe'–γ' pair gets closer to the inferred region of orthogonal pattern.

0.202, the same value as the reference model. As Pe' increased from 1.585 (corresponding to the spreading rate, v = 1 cm/year) to 4.756 (v = 3 cm/year), models with the higher resolutions exhibited the same transition with the reference grid spacing from the obliquely connecting to the orthogonal pattern (Fig. 11). The patterns varied from the orthogonal to overlapping when Pe' was further increased to 6.342 (v = 4 cm/year) (Fig. 11), as also seen in the models with the reference resolution.

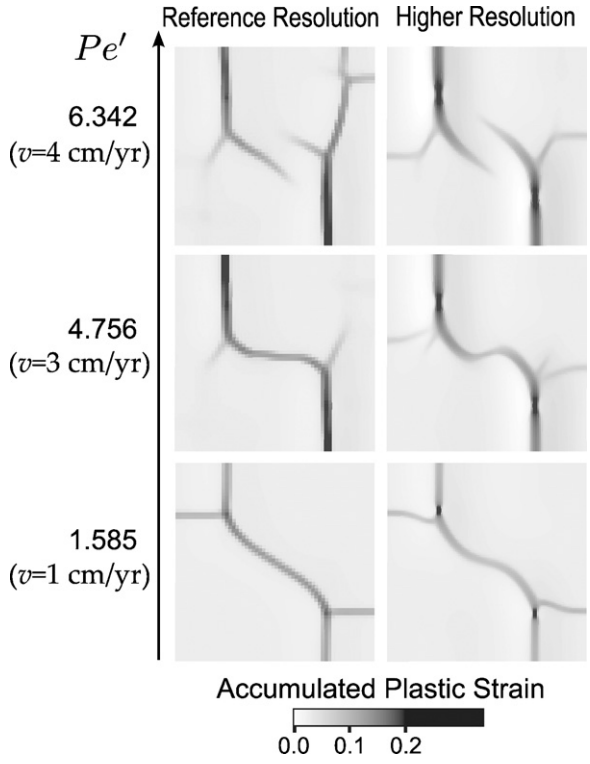

Fig. 11. Models with a twice higher horizontal resolution than those in Fig. 10. confirm that the transition of patterns occurs at consistent values of Pe'. The γ' of 0.202 was the same for all the compared models.

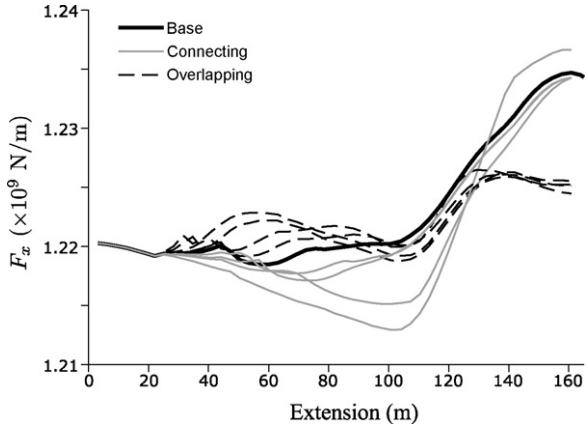

Fig. 12. For models with different weakening rates F_x is plotted as a function of the amount of extension. Models that are relatively slower in weakening (thin gray lines) develop larger differences between the lowest and the highest value in F_x and connecting-mode patterns emerge from them. In contrast, faster-weakening models (dashed lines) showed smaller differences between the lowest and the highest F_x and developed overlapping-mode patterns. This solid line corresponds to the "base" model, which developed an orthogonal pattern.

4.2. Variation in rate of weakening

The rate of strain weakening is another pattern-controlling factor. The eight models (W1–W8 in Table 1) share the two-stage weakening parameterization (Fig. 6), but differ in the rate of cohesion reduction. F_x-extension curves for these eight models are shown in Fig. 12. Models with higher ω consistently resulted in the overlapping patterns, while the connecting mode appeared in the models with lower ω. The map-view patterns from those models, taken after 10 kyears, are arranged in the order of increasing ω in Fig. 13, demonstrating the sensitivity of pattern to ω.

ω represents the amount of cohesion reduced after strain weakening occurred. Since the first appearance of localization from the seed elements is ridge segments that propagate in the direction perpendicular to the spreading direction, different values of ω have a prominent influence on that propagation. When a model has a higher ω while all other parameters remain the same compared to the base case, a lower level of cohesion is achieved and the propagation of ridge segments is facilitated. The net effect is equivalent to reducing γ by increasing the spreading rate, and the mode of interaction between two ridge segments becomes over-

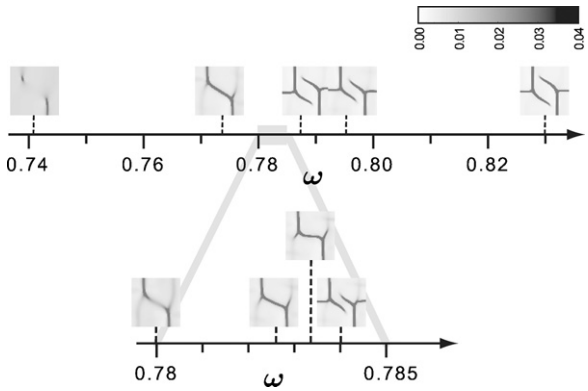

Fig. 13. Patterns of localized plastic strain on the top surface are arranged in the increasing order of ω. The smaller ω is, the larger is the cohesion at any point in accumulated plastic strain as long as cohesion is larger than 10% of its initial value (see Fig. 6). Patterns show the transition of patterns from high-θ connecting modes through the orthogonal pattern to overlapping modes as ω increases.

lapping. In contrast, when a model has a lower value of ω while all other parameters remain the same as the base model, the model remains at a relatively high level of cohesion and ridge propagation is hindered. As a result, a high-θ connecting mode emerges because the net effect is to raise γ by lowering the spreading rate.

5. Discussion and conclusion

Our model results are in good agreement with observations: as spreading rate (v) increases while all other variables remain constant, γ decreases and the mode of ridge interaction changes from connecting to overlapping. Consistent with this trend, orthogonal ridge-transform fault intersections are often found in the slow-spreading Mid-Atlantic Ridge (MAR). The overlapping mode of interaction would correspond to the formation of microplates, which are found only at the fastest spreading East Pacific Rise (EPR) (Naar and Hey, 1991). The large-θ connecting modes for the models at the lower end of Pe' appear to be relevant to the very-slow-spreading ridges (Dick et al., 2003). The Southwest Indian ridge (SWIR) between the Atlantis II and Gauss fracture zones, one of the very-slow-spreading oceanic ridges, shows a resemblance to the patterns of large-θ connecting mode seen in our low-γ models: segments that are normal to the spreading direction alternate with oblique ones (see Fig. 5a in Dick et al., 2003). According to Atwater and MacDonald (1977), observations show that slow spreading centers ($v < 3$ cm/year) are oblique to transform faults in most cases; spreading centers with intermediate rates ($v \approx 3$ cm/year) intersect transform faults both orthogonally and obliquely; only fast spreading centers ($v > 5$ cm/year) are nearly orthogonal to transform faults. Thus, it is consistent with these observations that the slow-spreading Southwest Indian ridge falls in the high-θ connecting-mode domain of the Pe'–γ' plot, while the intermediate-spreading mid-Atlantic ridge corresponds to the relatively low-θ near the field of orthogonal patterns (Fig. 10).

The deformation patterns found in the models are consistent with where actual ridge systems fall in the domain of Pe'–γ' (star symbols in Fig. 10). Assuming the same thermal parameters with the base case, the γ' value remains the same with that of the base case, 0.22, while the half-spreading rate (v) determines the value of Pe' and thus the position on the plot. The SWIR with $v = 1$ cm/year is located well within the high-θ connecting-mode domain; the MAR, spreading at $v = 2.5$ cm/year, falls in the low-θ connecting-mode region, implying that slight variations in thermal state or spreading rate can yield both orthogonal and obliquely connecting patterns; and the fast-spreading EPR ($v = 6$ cm/year) is in the overlapping-mode region.

It is possible that simplifications made in our model are the source of the discrepancy between modeling results and observations. For example, one of the factors that influence the localization pattern but was not addressed in this study is the offset between ridge segments. While observations on the newly formed oceanic basins support the discrete nucleation of spreading centers and their propagation as assumed in our model (e.g., Taylor et al., 1995), we did not take into account other characteristics inherited from the continental rifting phase. The size of our models is also fixed at the smallest possible for the first-order segmentation, and only the initial stage of pattern formation is considered. The mid-ocean ridge systems, however, exhibit a relatively wide range of ridge segment and transform fault lengths. They show a large amount of variability in the patterns of ridge-transform fault intersections, too. The EPR, for example, is "dominated" by overlapping segments but also has some orthogonal ones. The MAR has both orthogonal and oblique segments. The SWIR and the Gakkel ridge show the most striking variability implying that for the same spreading rate adjacent segments can be either orthogonal or oblique (M. Cannat, personal communication). However, it can be inferred from our model that segmentation is likely to be variable for one given spreading rate because factors such as magma supply rates, hydrothermal cooling and rheological properties are critical in determining the nature of segmentation and they are highly variable along axis as well as between mid-ocean ridge systems.

The assumed value of volumetric thermal expansion coefficient (α_v) needs further justification. Typical values of α_v for rocks composing oceanic crust are $(2–3) \times 10^{-5}\,K^{-1}$ (Turcotte and Schubert, 2001), whereas we take $6 \times 10^{-5}\,K^{-1}$ as a reference value. Volume change due to solidification is included in this larger value. Since oceanic crust was once melted and our initial temperature is well above the "elastic temperature limit" (~700 to 900 °C) (Reiter et al., 1987), we believe that it is essential to account for thermal stresses accumulated since the time of partial melt solidification, provided that newly formed oceanic crust can retain at least a portion of those stresses. If the liquid-to-solid phase change is taken into account, a jump in density (inversely proportional to volume change in case of mass conservation) is expected at the moment of phase transition (e.g., Kushiro, 1980). Below the elastic temperature limit, α_v becomes close to the conventional value. Thus, the value of α_v we used can be thought of as an average over the entire cooling process. One of the waxes that easily created the orthogonal patterns (Oldenburg and Brune, 1975), Shell Wax 200, is also characterized by a large density change from solidification and subsequent cooling (Sandwell, 1986).

Mantle upwelling patterns and their relation to along-axis segmentation have been studied extensively (e.g., Parmentier and Phipps Morgan, 1990; Shaw and Lin, 1996; Barnouin-Jha et al., 1997; Magde and Sparks, 1997; Choblet and Parmentier, 2001). However, the causal relation between them is not clear (Phipps Morgan, 1991). The time scale of mantle flow models is also significantly different from that of this study: it takes no longer than 10 kyears for the patterns of strain localization to emerge, while the time scale associated with mantle convection is typically on the order of million years. The segmentations were speculated to cause axial variations in mantle upwelling, not vice versa, because the patterns were made without the organized mantle upwelling in numerical experiments with an elastic damage model (Hieronymus, 2004). Our results support this point of view because the patterns were created without explicit consideration of mantle flow. Thus, we suggest that the patterns of ridge segments and transform faults are determined during the earliest period of spreading without substantial influence from mantle flow patterns. Later in time, the patterns are possibly modified by the change in plate motion, mantle upwelling, and magma supply.

Fracture zones were made in our models as a response to thermal stress. The thermal stress origin is consistent with previous analyses on thermal stress (Collette, 1974; Turcotte, 1974; Sandwell, 1986) and the role of ridge segments to release only the ridge-normal component of thermal stress assumed in this study. The orientation of their straight portion is parallel to the spreading direction as observed in mid-ocean ridge systems and wax experiments. The timing of fracture zone formation was always later than the emergence of patterns, which confirms the thermal origin of fracture zones because a sufficient amount of thermal stress alone would take longer to accumulate until yielding. Fracture zones were found to connect to the end of the non-connected branch of ridge segments rather than to extend in parallel from transform faults as most often found in the mid-ocean ridge systems (Fig. 4).

Similar patterns were found to emerge from 2D elastic damage models (Hieronymus, 2004). Comparable patterns included oblique 45°-connection (OC), transform fault (TF), and overlapping spreading centers (OSC). While keeping all other parameters the same as in their TF models, OCs require a stronger shear weakening due to "distortional energy" (defined as the double contraction of deviatoric stress and deviatoric strain tensors), while OSCs need a larger tensile strain as well as zero contribution to shear weakening from the distortional energy and the second invariant of deviatoric stress. The importance of the amount of tensile strain is comparable to our results: larger applied strains correspond to faster spreading rates in terms of emergent patterns. Adjusting their damage properties roughly corresponds to varying our strain-weakening parameter, ω. However, the fundamental difference from our study is their emphasis on material properties rather than loading conditions. Although it was implied that different oceanic lithospheres are composed of inherently different materials, Hieronymus's study did not address the reason and processes responsible for such heterogeneity. On the contrary, we showed that the inclusion of thermal stresses is critical to determining the patterns in the mid-ocean ridge systems and that the differently loaded ridge systems can produce different patterns even for the same material properties. This allows our work to be more closely linked to the underlying physics as well as previous works which invoked thermal stress as the key driving force in mid-ocean ridge segmentation (Oldenburg and Brune, 1972, 1975; Collette, 1974; Turcotte, 1974; Sandwell, 1986). We note that rheology and loading, the two fundamental aspects of continuum mechanical problems, are not mutually exclusive. In the future it would be desirable to adopt an elasto-plasticity combined with sophisticated damage models.

In summary, we showed that selectively released thermal stress can be a significant source of ridge-parallel tension. Numerical thermo-mechanical models showed that the resultant ridge-parallel tension from cooling and ridge-normal extension by far-field tectonic forces together create variation in the mode of interaction between two mutually approaching ridge segments. The ratio of thermal stress to spreading-induced stress is a first-order measure of the mode that subsequently develops. When the rates of each driving process are measured separately, the models were clearly divided into different modes of interaction. In general, the larger ratio of thermal stress to spreading-induced stress leads to the connecting mode, while the smaller ratio to the overlapping one. This correlation can translate to the observed correlation between the spreading rate and the modes of intersection between spreading centers and transforms faults. Magma-supply models have been successful in explaining the along-axis variability of mid-ocean ridge systems. Factors considered significant in those models such as magma supply rate and hydrothermal cooling eventually give rise to the local variations in thermal state. In that sense, our thermo-mechanical model would be complementary to such a long-term mode. A better understanding of the segmentation of the mid-ocean ridge systems would come from longer-term models that incorporate the continental rifting and magma supply models. In light of the high sensitivity of models to strain-weakening rates, it would be also crucial to use geologically constrained plastic parameters.

Acknowledgements

This is contribution number 9149 of the Division of Geological and Planetary Sciences and 41 of the Tectonics Observatory. Development of SNAC was partially supported by the NSF ITR program under EAR-0205653. All calculations carried out on the Caltech Geosciences Supercomputer Facility partially supported by NSF EAR-0521699. Additional support provided through the Caltech Tectonics Observatory by the Gordon and Betty Moore Foundation.

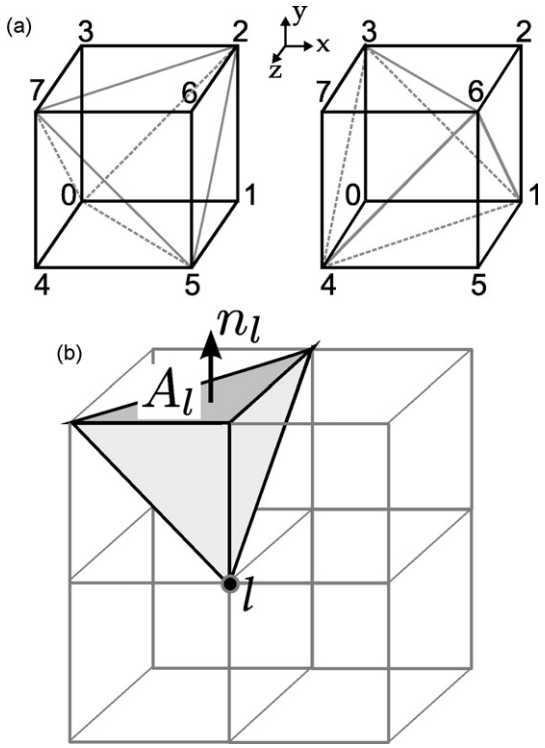

Fig. A1. (a) Two configurations of five tetrahedra in a hexahedral element used in the mixed discretization. Numbers next to apexes indicate the local node numbering. (b) Conventions for the notation. A_l and n_l denote the face and the unit normal vector, respectively, associated with a node l.

Appendix A. Algorithm of SNAC

A.1. Governing equations

The software package SNAC solves the momentum and the heat energy balance equations in the following differential form:

$$\frac{\partial \sigma_{ij}}{\partial x_j} + \rho g_i = \rho \frac{\mathrm{D}v_i}{\mathrm{D}t}, \tag{A.1}$$

$$\frac{\partial q_i}{\partial x_i} + r = \rho C_p \frac{\mathrm{D}T}{\mathrm{D}t}. \tag{A.2}$$

In the momentum balance equation, ρ is the mass density, v_i is velocity, σ_{ij} is the Cauchy stress tensor, and g_i is the gravitational acceleration. T is temperature, C_p is the specific heat at constant pressure, q_i is the heat flux vector, and r is the volumetric heat source. D/Dt represents the material time derivative. In this study, no heat sources are considered, including shear heating. Viscosity is temperature- and/or stress-dependent. The elastic component of stress has an extra contribution from thermal stress.

A.2. Spatial discretization

A 3D domain is discretized into hexahedral elements, each of which is filled with two sets of five tetrahedra (Fig. A1a). In this mesh hierarchy, called the mixed discretization (Marti and Cundall, 1982), hexahedral elements are used only as an averaging unit for volumetric strain. The averaging is enforced at all times, for incompressible viscoelastic or plastic constitutive laws. For a given

loading, responses of one set of tetrahedra can be different from those of the other set because of the differently orientated faces of tetrahedra in each set (e.g., Zienkiewicz et al., 1995). So, the use of two equivalent sets of tetrahedra is required to ensure a symmetric response.

The approximation of partial derivatives with respect to spatial variables follows the integral definitions (e.g., Wilkins, 1964):

$$\int_{\Omega} f_{,i}\,\mathrm{d}V = \int_{\partial\Omega} f n_i\,\mathrm{d}\Gamma, \tag{A.3}$$

where Ω represents a tetrahedron as an integration domain, $\partial\Omega$ is the boundary surfaces of the tetrahedron, f_i is the partial derivative of a variable f with respect to ith spatial coordinate, n_i is the ith component of the unit normal vector of the surface. If the partial derivative is constant within a tetrahedron, it is evaluated as

$$f_{,i} = \frac{1}{V}\int_{\partial\Omega} f n_i\,\mathrm{d}\Gamma, \tag{A.4}$$

where V is the volume of the tetrahedron. By further substituting an algebraic expression for the surface integral, reordering terms, and using $\int_{\partial\Omega} n_i\,\mathrm{d}\Gamma = 0$ (when $f = 1$ in (A.4)):

$$f_{,i} = \frac{1}{V}\sum_{l=1}^{4}\bar{f}^l n_i^l A^l = \frac{1}{V}\sum_{l=1}^{4}\frac{1}{3}\sum_{m=1,\,\neq l}^{4} f^m n_i^l A^l = \frac{1}{3V}\sum_{m=1}^{4} f^m \sum_{l=1,\,\neq m}^{4} n_i^l A^l$$

$$= -\frac{1}{3V}\sum_{m=1}^{4} f^m n_i^m A^m, \tag{A.5}$$

where l is the local node index varying from 1 to 4, A^l and n^l are the area and the unit normal vector of the triangular surface not having the node l as one of its apexes (Fig. A1b). Hereafter, we call such a face a *corresponding* face to node l. $\bar{f}^l$ is the averaged f on the surface l.

A.3. Nodal assemblage

We can convert the differential equation for momentum balance (A.1) (the following description is applied to the heat equation in the same fashion) to a principle of minimum work rate as in the standard finite element formulation:

$$\int_{\Omega} \delta v_i \rho \frac{\mathrm{D}v_i}{\mathrm{D}t}\,\mathrm{d}V = \int_{\Omega} \delta v_i \rho g_i\,\mathrm{d}V + \int_{\Omega} \delta\xi_{ij}\sigma_{ij}\,\mathrm{d}V, \tag{A.6}$$

where ξ_{ij} are components of the strain rate tensor, δv_i and $\delta\xi_{ij}$ represent variations of velocity and strain rate, and Ω here corresponds to the whole domain. The local contribution to nodes corresponding to each term can be computed by following the standard finite element procedure for linear tetrahedral elements. However, our method does not need to construct coefficient matrices such as mass and stiffness matrices since it adopts an explicit time discretization. The resultant momentum equation is

$$M^n \frac{\mathrm{D}v_i^n}{\mathrm{D}t} = \frac{1}{3}T_i^{[n]} + \frac{1}{4}\rho^{[n]} g_i V^{[n]}, \tag{A.7}$$

where the superscript n represents values evaluated at the global node n, the superscript $[n]$ means the sum of contributions from all the tetrahedra having the global node n as an apex, T_i is the traction that is defined as $\sigma_{ij}n_j$ and evaluated on a face of one of the contributing tetrahedra. The nodal mass M^n is not the actual inertial mass but an adjusted one to satisfy a local stability criterion discussed in the Section A.5. The correspondence between an apex and a face for the traction calculation is determined as in the derivation of the expression (A.5). Note that the factor of 1/3 in the traction term is inherited from (A.5) and the factor of 1/4 in the body force term implies that the nodal contribution takes one quarter of a tetrahedron's volume-dependent quantity.

While looping over the entire set of nodes, mass and nodal forces are assembled by adding up the contributions from boundary conditions and all the tetrahedra sharing that node as one of their apexes. The structured mesh of SNAC renders the assemblage step conveniently static. The acquired net force (or heat flux) at each node is used to update velocities and node coordinates (or temperature.)

A.4. Damping and explicit time marching

We seek static or quasi-static solutions through a dynamic relaxation method. Instead of adding a usual velocity-dependent friction term, we adopt a local non-viscous damping scheme (Cundall, 1987):

$$F_i^{\mathrm{damped}} = F_i - \alpha\ \mathrm{sgn}(v_i)|F_i|, \tag{A.8}$$

where F_i is the ith component of the residual force vector, α is a positive coefficient less than 1, $\mathrm{sgn}(v_i)$ returns the sign of the i-th component of velocity, v_i. Once net forces are assembled and damped, velocity and displacement at that node are updated using a forward Euler method:

$$v\left(t+\frac{\Delta t}{2}\right) = v\left(t-\frac{\Delta t}{2}\right) + \Delta t\frac{F_i^{\mathrm{damped}}}{M}, \tag{A.9}$$

$$x(t+\Delta t) = x(t) + \Delta t v\left(t+\frac{\Delta t}{2}\right). \tag{A.10}$$

Damping is irrelevant to the update of temperature field, but the same forward Euler method is used.

A.5. Mass scaling for numerical stability

The conventional Courant–Friedrichs–Lewy (CFL) condition imposes a stringent upper limit for the time step size such that dynamic relaxation takes long time to get quasi-static solution over a geological time scale. To overcome this limit, a mass scaling technique is applied. This technique adjusts each nodal mass such that the stability condition for a user-specified time step can be locally satisfied. The stability condition to be satisfied, however, is not the same as in the CFL condition, i.e., $\Delta t \le (l_{\min}/v_{\mathrm{p}})$, where Δt is the time step, $l_{\min}$ is the minimum element size, and v_{p} is the P wave velocity. Instead, through an analogy of continuum to an infinite mass-spring system, we use a criterion that does not explicitly include length scale and P wave velocity (see Chapter 9 in Bathe, 1996):

$$\Delta t \le \frac{T}{\pi}, \tag{A.11}$$

where T is the period of system, $2\pi(m/k)^{1/2}$, m is a point mass, and k is the stiffness of the spring attached to the point mass. Now, reducing the infinite series of mass and springs in one dimension to a single mass-spring system, the stiffness of that single system becomes $4k$, leading to an expression for the mass scaling:

$$m \ge k(\Delta t)^2 \tag{A.12}$$

For a given size of Δt, the nodal mass is adjusted according to (A.12) to automatically satisfy the stability criteria (A.11). The value of k is computed by equating internal force contribution at a node with $-ku_i$:

$$\frac{1}{3}T_i = -ku_i \Rightarrow$$
$$\frac{1}{3}(\lambda+2\mu)(\dot{\varepsilon}_{ii}\,\mathrm{d}t)n_i S = -k(v_i\,\mathrm{d}t)\,(\text{no sum}), \tag{A.13}$$

where only the volumetric contribution from internal forces is taken into account. By substituting the approximation for the partial derivative (A.5) into the above equation and dividing both sides by $v_i\,dt$, we obtain

$$k_i^l = \frac{1}{9V}(\lambda + 2\mu)(n_i^l S^l)^2, \tag{A.14}$$

where l is the local index for apexes of a tetrahedron and the surface-related quantities are computed on the corresponding face of the tetrahedron. Finally, a tetrahedron's contribution to the scaled mass is given as

$$m^l = \frac{\lambda + 2\mu}{9V}\max[(n_i^l S^l)^2, i = 1, \ldots, 3] \tag{A.15}$$

As in the standard FEM, appropriate mappings between local and global indices are required.

A.6. Constitutive update

SNAC uses a general elasto-visco-plastic rheological model to update the Cauchy stress tensor (e.g., Albert et al., 2000). First, the initial guess of stress is acquired by the Maxwell viscoelastic constitutive law (Poliakov et al., 1993). If this initial guess exceeds a given yield stress, it is projected onto the yield surface using a return mapping method (Simo and Hughes, 2004); otherwise, the viscoelastic stress update is retained. This elasto-visco-plastic model can deal with various constitutive laws that are typically used for the Earth's crustal and mantle material as its limiting cases. For example, elastic, viscoelastic and elastoplastic material are realized in the following cases:

1. Elastic material corresponds to the limit of infinite viscosity and yield stress.
2. Viscoelastic material corresponds to the limit of infinite yield strength.
3. Elasoplastic material corresponds to the inifinte viscosity.

Using the viscoplastic rheology is physically more realistic than using one of the limiting cases listed above since all materials have dissipative mechanisms and hence viscosity. This viscosity also provides a length scale for the problem of localization, which in turn enables physically meaningful mesh independent solution when the mesh size is smaller than this length scale.

Since the nodal variables are velocities and whose spatial gradients are deformation rates, we formulate the constitutive update in terms of strain rate. The objective stress rate of choice is the Jaumann or the corotational stress rate ($\Delta\sigma^{\Delta J}$) (Rudnicki and Rice, 1975):

$$\Delta\sigma^{\Delta J} = \frac{\partial(\Delta\sigma)}{\partial t} - W\,\Delta\sigma - \Delta\sigma\,W^{\mathrm{T}}, \tag{A.16}$$

where $W_{ij} = (1/2)(\partial v_i/\partial x_j - \partial v_j/\partial x_i)$ are the components of spin tensor and $\Delta\sigma$ is the increment of stress tensor. Correction to the stresses due to rotation can be given as

$$\sigma^{t+\Delta t} = \sigma^t + \Delta\sigma^{\Delta J}\,\Delta t \tag{A.17}$$

References

Abelson, M., Agnon, A., 1997. Mechanics of oblique spreading and ridge segmentation. Earth Planet. Sci. Lett. 148 (3/4), 405–421.

Albert, R., Phillips, R., Dombard, A., Brown, C., 2000. A test of the validity of yield strength envelope with an elastoviscoplastic finite element model. Geophys. J. Int. 140, 399–409.

Atwater, T., MacDonald, K.C., 1977. Are spreading centres perpendicular to their transform faults? Nature 270 (5639), 715–719.

Barnouin-Jha, K., Parmentier, E., Sparks, D., 1997. Buoyant mantle upwelling and crustal production at oceanic spreading centers: on-axis segmentation and off-axis melting. J. Geophys. Res. 102 (B6), 11979–11989.

Bathe, K.-J., 1996. Finite Element Procedure. Prentice-Hall, Upper Saddle River, NJ.

Behn, M.D., Lin, J., 2000. Segmentation in gravity and magnetic anomalies along the U.S. east coast passive margin; implications for incipient structure of the oceanic lithosphere. J. Geophys. Res. 105 (11), 25769–25790.

Behn, M.D., Lin, J., Zuber, M.T., 2002. Evidence for weak oceanic transform faults. Geophys. Res. Lett. 29 (24), 2207, doi:10.1029/2002GL015612.

Bergman, E., Solomon, S., 1984. Source mechanisms of earthquakes near mid-ocean ridges from body waveform inversion: implications for the early evolution of oceanic lithosphere. J. Geophys. Res. 89 (B13), 11415–11441.

Boley, B., Weiner, J., 1960. Theory of Thermal Stresses. Wiley, New York.

Choblet, G., Parmentier, E., 2001. Mantle upwelling and melting beneath slow spreading centers: effects of variable rheology and melt productivity. Earth Planet. Sci. Lett. 184, 589–604.

Cochran, J.R., Martinez, F., 1988. Evidence from the northern Red Sea on the transition from continental to oceanic rifting. Tectonophysics 153 (1–4), 25–53.

Collette, B., 1974. Thermal contraction joints in a spreading seafloor as origin of fracture zones. Nature 251, 299–300.

Cundall, P.A., 1987. Distinct element models of rock and soil structure. In: Brown, E.T. (Ed.), Analytical and Computational Methods in Engineering Rock Mechanics. Allen & Unwin, London, pp. 129–163 (Chapter 4).

Dick, H.J., Lin, J., Schouten, H., 2003. An ultraslow-spreading class of ocean ridge. Nature 426 (6965), 405–412.

Fox, P., Gallo, D., 1984. A tectonic model for ridge-transform-ridge plate boundaries: implications for the structure of oceanic lithosphere. Tectonophysics 104, 205–242.

Froidevaux, C., 1973. Dissipation and geometric structure at spreading plate boundaries. Earth Planet. Sci. Lett. 20 (3), 419–424.

Fujita, K., Sleep, N.H., 1978. Membrane stresses near mid-ocean ridge-transform intersections. Tectonophysics 50 (2/3), 207–221.

Furlong, K., Sheaffer, S., Malservisi, R., 2001. Thermal–rheological controls on deformation within oceanic transforms. In: Holdsworth, R., Strachan, R., Magloughlin, J., Knipe, R. (Eds.), The Nature and Tectonic Significance of Fault Zone Weakening, vol. 186. Geological Society, London, pp. 65–83.

Grindlay, N.R., Fox, P.J., 1993. Lithospheric stresses associated with nontransform offsets of the mid-Atlantic Ridge—implications from a finite-element analysis. Tectonics 12 (4), 982–1003.

Gudmundsson, A., 1995. Stress fields associated with oceanic transform faults. Earth Planet. Sci. Lett. 136 (3/4), 603–614.

Gurnis, M., Hall, C., Lavier, L., 2004. Evolving force balance during incipient subduction. Geochem. Geophys. Geosyst. 5, Q07001, doi:10.1029/2003GC000681.

Haxby, W.F., Parmentier, E.M., 1988. Thermal contraction and the state of stress in the oceanic lithosphere. J. Geophys. Res. 93 (6), 6419–6429.

Hieronymus, C., 2004. Control on seafloor spreading geometries by stress- and strain-induced lithospheric weakening. Earth Planet. Sci. Lett. 222, 177–189.

Katz, R.F., Ragnarsson, R., Bodenschatz, E., 2005. Tectonic microplates in a wax model of sea-floor spreading. New J. Phys. 7 (37), doi:10.1088/1367-2630/7/1/037.

Kushiro, I., 1980. Viscosity, density, and structure of silicate melts at high pressures, and their petrological applications. In: Hargraves, R.B. (Ed.), Physics of Magmatic Processes. Princeton University Press, Princeton.

Lachenbruch, A.H., 1973. A simple mechanical model for oceanic spreading center. J. Geophys. Res. 78 (17), 3395–3413.

Lavier, L.L., Buck, W., 2002. Half graben versus large-offset low-angle normal fault: importance of keeping cool during normal faulting. J. Geophys. Res. 107 (B6), 2122, doi:10.1029/2001JB000513.

Lavier, L.L., Buck, W.R., Poliakov, A.N.B., 2000. Factors controlling normal fault offset in an ideal brittle layer. J. Geophys. Res. 105 (B10), 23431–23442.

Macdonald, K., Scheirer, D., Carbotte, S., 1991. Mid-ocean ridges: discontinuities, segments and giant cracks. Science 253 (5023), 986–994.

Magde, L., Sparks, D., 1997. Three-dimensional mantle upwelling, melt generation, and melt migration beneath segment slow spreading ridges. J. Geophys. Res. 102 (B9), 20571–20583.

Marti, J., Cundall, P., 1982. Mixed discretization procecure for accurate modelling of plastic collapse. Int. J. Numer. Anal. Methods Geomech. 6, 129–139.

McClay, K., Khalil, S., 1998. Extensional hard linkages, eastern Gulf of Suez, Egypt. Geology 26 (6), 563–566.

Menard, H.W., Atwater, T., 1969. Origin of fracture zone topography. Nature 222 (5198), 1037–1040.

Naar, D.F., Hey, R.N., 1991. Tectonic evolution of the Easter microplate. J. Geophys. Res. 96 (5), 7961–7993.

Oldenburg, D., Brune, J., 1975. An explanation for the orthogonality of ocean ridges and transform faults. J. Geophys. Res. 80 (17), 2575–2585.

Oldenburg, D.W., Brune, J.N., 1972. Ridge transform fault spreading pattern in freezing wax. Science 178 (4058), 301–304.

Parmentier, E., Phipps Morgan, J., 1990. Spreading rate dependence of three-dimensional structure in oceanic spreading centres. Nature 348, 325–328.

Parmentier, E.M., Haxby, W.F., 1986. Thermal stresses in the oceanic lithosphere: evidence from geoid anomalies at fracture zones. J. Geophys. Res. 91 (7), 7193–7204.

Phipps Morgan, J., 1991. Mid-ocean ridge dynamics—observations and theory. Rev. Geophys. Suppl. 29, 807–822.

Poliakov, A.N.B., Cundall, P.A., Podladchikov, Y.Y., Lyakhovsky, V.A., 1993. An explicit inertial method for the simulation of viscoelastic flow: an evaluation of elastic effects on diapiric flow in two- and three-layers models. In: Flow and Creep in the Solar Systems: Observations, Modeling and Theory. Kluwer Academic Publishers, pp. 175–195.

Reiter, M., Barroll, M.W., Minier, J., Clarkson, G., 1987. Thermo-mechanical model for incremental fracturing in cooling lava flows. Tectonophysics 142, 241–260.
Rudnicki, J., Rice, J., 1975. Conditions for the localization of deformation in pressure-sensitive dilatant materials. J. Mech. Phys. Solids 23, 371–394.
Sandwell, D., 1986. Thermal stress and the spacings of transform faults. J. Geophys. Res. 91 (B6), 6405–6417.
Scholz, C.H., 2002. The Mechanics of Earthquakes and Faulting, 2nd edition. Cambridge University Press.
Shaw, W., Lin, J., 1996. Models of ocean ridge lithospheric deformation: dependence on crustal thickness, spreading rate, and segmentation. J. Geophys. Res. 101 (B8), 17977–17993.
Simo, J., Hughes, T., 2004. Computational Inelasticity. Springer, New York.
Taylor, B., Goodliffe, A.M., Martinez, F., Hey, R.N., 1995. Continental rifting and initial sea-floor spreading in the Woodlark Basin. Nature 374 (6522), 534–537.
Turcotte, D., 1974. Are transform faults thermal contraction cracks? J. Geophys. Res. 79 (17), 2573–2577.
Turcotte, D.L., Schubert, G., 2001. Geodynamics, 2nd edition. Cambridge University Press.
Watts, A.B., 2001. Isostasy and Flexure of the Lithosphere. Cambridge University Press.
Watts, A.B., Stewart, J., 1998. Gravity anomalies and segmentation of the continental margin offshore West Africa. Earth Planet. Sci. Lett. 156 (3/4), 239–252.
Wiens, D.A., Stein, S.A., 1984. Intraplate seismicity and stresses in young oceanic lithosphere. J. Geophys. Res. 89 (13), 11442–11464.
Wilkins, M.L., 1964. Calculation of elastic–plastic flow. Methods Comput. Phys. 3, 211–263.
Wilson, J.T., 1965. A new class of faults and their bearing on continental drift. Nature 207 (4995), 343–347.
Zienkiewicz, O.C., Huang, M., Pastor, M., 1995. Localization problems in plasticity using finite elements with adaptive remeshing. Int. J. Numer. Anal. Methods Geomech. 19, 127–148.